

# High Perceptual Quality Image Denoising with a Posterior Sampling CGAN

Guy Ohayon  
Technion

Theo Adrai  
Technion

Gregory Vaksman  
Technion

Michael Elad  
Google Research

Peyman Milanfar  
Google Research

## Abstract

*The vast work in Deep Learning (DL) has led to a leap in image denoising research. Most DL solutions for this task have chosen to put their efforts on the denoiser’s architecture while maximizing distortion performance. However, distortion driven solutions lead to blurry results with sub-optimal perceptual quality, especially in immoderate noise levels. In this paper we propose a different perspective, aiming to produce sharp and visually pleasing denoised images that are still faithful to their clean sources. Formally, our goal is to achieve high perceptual quality with acceptable distortion. This is attained by a stochastic denoiser that samples from the posterior distribution, trained as a generator in the framework of conditional generative adversarial networks (CGANs). Contrary to distortion-based regularization terms that conflict with perceptual quality, we introduce to the CGANs objective a theoretically founded penalty term that does not force a distortion requirement on individual samples, but rather on their mean. We showcase our proposed method with a novel denoiser architecture that achieves the reformed denoising goal and produces vivid and diverse outcomes in immoderate noise levels.*

## 1. Introduction

Image denoising is one of the most fundamental problems in image processing, and as such it has been explored quite extensively. As deep learning emerged in the past decade, many neural-network-based attempts were made to solve this task. These led to state-of-the-art (SoTA) performance in commonly used full reference *distortion* measures, such as Mean-Squared-Error (MSE), that quantify the discrepancy between the denoised image and its clean source [32, 33, 27, 24, 25, 31]. While optimizing a distortion measure leads to denoised images that are faithful to their clean sources, the *perceptual quality*, which is the degree to which a denoised image looks natural, is also an important measure to consider. Recent work has tried to achieve higher perceptual quality compared to distortion based solutions by concurrently optimizing both measures [7, 8]. However, these attempts achieve sub-optimal

perceptual quality [5], and there are hardly any deep learning solutions that address the image denoising problem while targeting optimal perceptual performance.

In this work we seek to obtain a denoiser that achieves very high perceptual quality, while accompanied by a guarantee on its distortion performance. As shown in [5], sampling from the posterior distribution achieves such a goal, compromising 3dB on the optimal Peak Signal To Noise Ratio (PSNR) performance, making such a stochastic denoiser an excellent candidate for our needs. The idea of using posterior sampling for solving image restoration tasks has already been suggested in various contexts [23, 26, 1]. Although high dimensional posterior sampling is still considered as a challenging task, recent deep learning methods seem to provide practical tools for handling it.

The success of generative adversarial networks (GANs) has led authors to incorporate sampling (not necessarily from the posterior distribution) to solve various image restoration tasks on certain classes of images [3, 19, 4, 28], and to excellent sampling capabilities from class-specific priors [14, 15]. Most of these were possible due to the improvements in the generative adversarial learning scheme [16, 2, 10] that allowed stable training, contrary to the instabilities of the originally proposed GAN optimization objective [9]. The authors of [1] have shown that the CGAN objective [20] formalized under the Wasserstein-1 metric [10, 2] theoretically drives a conditional generator to sample from the posterior distribution. Therefore, such an optimization framework provides a practical way to approximate the desired sampling. For instance, the Latent Adversarial Generator (LAG) [4] has shown SoTA single image super resolution results from an extremely low resolution input, attained by a tweaked version of CGAN.

Rather than seeking a balance between perceptual quality and distortion performance, we aim to sample from the posterior distribution while willing to compromise up to 3dB in PSNR performance. In order to regularize the proposed sampling, we leverage the property that any stochastic denoiser that samples from such a distribution must also agree in expectation with it. We introduce a term to the CGAN objective that penalizes solutions which do not satisfy such a necessary property. Unlike other related

methods, our regularization term does not force a distortion requirement on individual denoised samples, but rather on their mean. Our proposed denoiser’s architecture is a novel encoder-decoder, inspired by StyleGAN2 [14] and UNet [21], with a high receptive field and a noise injection scheme generalizing that of StyleGAN [15]. We showcase the capabilities of our proposed method in high noise conditions, basing our experiments on several data sets.

## 2. Proposed Method: Derivations

Assume an unknown distribution of images  $\mathbb{P}_x$  and a known stochastic degradation operator  $\text{deg}(\cdot)$  (such as additive Gaussian noise). Our goal is to sample from the posterior distribution  $\mathbb{P}_{x|y}$  with the help of an independent random vector  $z$  of known distribution. We assume that given  $y = \text{deg}(x)$ , a degraded observation of  $x$ , there exists a parametric mapping  $g_\theta = G_\theta(z, y)$  such that  $z \sim \mathbb{P}_z$ ,  $g_\theta|y \sim \mathbb{P}_{x|y}$ , and  $\mathbb{P}_z$  is a known latent distribution where  $z$  and  $y$  are mutually independent.

For a given  $y = y$  (denoting  $y$  as a realization of the random variable  $y$ ), the Wasserstein-1 distance [2] between  $\mathbb{P}_{g_\theta|y=y}$  and  $\mathbb{P}_{x|y=y}$  can be shown to satisfy the equality

$$\begin{aligned} & W_1(\mathbb{P}_{x|y=y}, \mathbb{P}_{g_\theta|y=y}) \\ &= \sup_{f \in L_1} \mathbb{E}_{x|y} [f(x, y)] - \mathbb{E}_{g_\theta|y} [f(g_\theta, y)], \end{aligned} \quad (1)$$

where  $L_1$  is the set of all functions  $f : \mathcal{X} \times \mathcal{Y} \rightarrow \mathbb{R}$  that are 1-Lipschitz on  $\mathcal{X}$  for any  $y \in \mathcal{Y}$ . Observe that (1) is defined for a given realization of  $y$ , whereas we seek an optimization objective that considers all possible ones. This can be accomplished by taking an expectation on both sides with respect to  $y$ . The work in [1] shows that such an expectation taken on the right hand side in (1) commutes with the supremum, leading to

$$\begin{aligned} & \mathbb{E}_y [W_1(\mathbb{P}_{g_\theta|y}, \mathbb{P}_{x|y})] \\ &= \sup_{f \in L_1} \mathbb{E}_{x,y} [f(x, y)] - \mathbb{E}_{g_\theta,y} [f(g_\theta, y)]. \end{aligned} \quad (2)$$

Observe that contrary to (1), the expectations in (2) act on the joint distributions  $\mathbb{P}_{x,y}$  and  $\mathbb{P}_{g_\theta,y}$ . Therefore, assuming that the function  $f$  in the supremum of (2) can be found for each  $y$ , one could evaluate this distance as follows:

- Draw samples of  $x \sim \mathbb{P}_x$  (e.g., get an image data set).
- Perform  $y = \text{deg}(x)$  on each sample of  $x$ , to obtain samples of  $y$  (e.g., contaminate with noise).
- Draw independently samples of  $z \sim \mathbb{P}_z$ .
- Compute  $G_\theta(z, y)$  on each sample of  $y$  and  $z$ , to obtain samples of  $g_\theta$  (e.g., denoise each noisy image with a stochastic denoiser).
- We now have samples drawn from both  $\mathbb{P}_{x,y}$  and  $\mathbb{P}_{g_\theta,y}$ . Evaluate (2) using the law of large numbers.

Considering  $G_\theta(z, y)$  as a generator and assuming that  $f$  is somehow realized for each  $\theta$ , we could optimize for  $\theta$ :

$$\begin{aligned} & \min_{\theta} \mathcal{L}(\mathbb{P}_{x|y}, \mathbb{P}_{g_\theta|y}) \\ &= \min_{\theta} \sup_{f \in L_1} \mathbb{E}_{x,y} [f(x, y)] - \mathbb{E}_{g_\theta,y} [f(g_\theta, y)]. \end{aligned} \quad (3)$$

If  $f$  is a parametrized critic, this is a game between two adversaries, having a classic GAN structure. While this optimization task may seem appealing and practical, it is in fact ill-posed since we are confined to a finite size and unbalanced data-set, in which for each  $x$  we have many  $y$ ’s but not vice versa. A generator optimized under (3) with such data would try to learn to sample from the posterior distribution  $\mathbb{P}_{x|y}$  with only one sample from  $x|y$  for each  $y$ . This would most likely lead to mode collapse [9, 12, 18, 29], where  $g_\theta|y$  becomes a degenerate random variable and the generator ignores  $z$ , since for each conditional input  $y$  it is sufficient for the generator to produce only one image that is acceptable by the critic. Hence, the densities  $\mathbb{P}_{g_\theta|y}$  and  $\mathbb{P}_{x|y}$  might be equal only on this finite number of points, while allowing a deviation in the remaining domain. To alleviate this weakness, we add a constraint to (3) as follows:

$$\begin{aligned} & \min_{\theta} \mathcal{L}(\mathbb{P}_{x|y}, \mathbb{P}_{g_\theta|y}) \\ & \text{s.t. } \mathbb{E}_{x,y} [\|x - \mathbb{E}[g_\theta|y]\|_2^2] = \mathbb{E}_y [\text{Var}(x|y)]. \end{aligned} \quad (4)$$

Observe that if there exists  $\theta^*$  such that  $p_{g_{\theta^*}|y} = p_{x|y}$ , then  $\theta^*$  is a global optimum of task (3), implying that the distance between the two conditional distributions is zero. In addition,  $\theta^*$  remains the global optimum of task (4) since  $p_{g_{\theta^*}|y} = p_{x|y}$  implies that  $\mathbb{E}[g_{\theta^*}|y] = \mathbb{E}[x|y]$ , and thus  $\mathbb{E}_{x,y} [\|x - \mathbb{E}[g_{\theta^*}|y]\|_2^2] = \mathbb{E}_{x,y} [\|x - \mathbb{E}[x|y]\|_2^2] = \mathbb{E}_y [\text{Var}(x|y)]$ , which is the Minimum Mean Squared Error (MMSE). Thus, the added constraint is also satisfied by  $\theta^*$ , which means that it is a necessary condition on any solution that yields  $p_{g_{\theta^*}|y} = p_{x|y}$ . In other words, instead of having distortion requirements on specific samples (as in LAG [4] for instance), we require an agreement with the expectation of the posterior, i.e., the constraint enforces many samples of  $g_\theta|y$  to agree with  $x|y$  (in expectation). As we will see in Section 4, this revision leads to a stochastic variation and therefore circumvents mode collapse.

Since  $\mathbb{E}[\text{Var}(x|y)]$  is the global minimum of  $\mathbb{E}[\|x - \mathbb{E}[g_\theta|y]\|_2^2]$ , we can reformulate the optimization of task (4) by adding a penalty term to task (3):

$$\min_{\theta} \mathcal{L}(\mathbb{P}_{x|y}, \mathbb{P}_{g_\theta|y}) + \lambda \mathbb{E} [\|x - \mathbb{E}[g_\theta|y]\|_2^2]. \quad (5)$$

The posterior distribution is still a globally optimal solution to this problem, since both expressions admit their minimum for the same  $\theta^*$ . This way, the proposed scheme eliminates many possible solutions that might minimize the first term but are far from the true posterior.

At first glance, LAG [4] could also seem like a method that directly aims for the perceptual quality goal. LAG’s objective is almost identical to that of CGAN, with an additional generator regularization term:

$$\min_{\theta} \mathcal{L}(\mathbb{P}_{\mathbf{x}|\mathbf{y}}, \mathbb{P}_{\mathbf{g}_{\theta}|\mathbf{y}}) + \lambda \mathbb{E}_{\mathbf{x}, \mathbf{y}} [\|P(\mathbf{x}, \mathbf{y}) - P(G_{\theta}(0, \mathbf{y}), \mathbf{y})\|_2^2]. \quad (6)$$

In LAG, the function  $P(\cdot, \cdot)$  in the above expression represents a part of the critic that extract features from the image pair fed to it. This function could be considered as a variant or part of the function  $f$  we have used above. Referring to the second term, its rationale is the belief that the intermediate representations of  $(\mathbf{x}, \mathbf{y})$  and  $(G_{\theta}(0, \mathbf{y}), \mathbf{y})$  are necessarily close-by. Observe that this penalty is substantially different from the expectation requirement we have posed in equation (5), since we do not assume that a given sample (i.e., the one attained at  $\mathbf{z} = 0$ ) and  $\mathbf{x}$  are matched in distortion. When  $G_{\theta}(\cdot, \cdot)$  and  $P(\cdot, \cdot)$  are continuous mappings, this assumption poses a distortion requirement not only on  $G_{\theta}(0, \mathbf{y})$ , but also on its neighbourhood, which happens to be the most likely samples produced when  $\mathbf{z}$  is Gaussian with zero mean (as in LAG). Thus, the penalty term in (6) conflicts with the perceptual quality goal [5], whereas the penalty term we propose in (5) does not.

### 3. Proposed Method: Details

#### 3.1. Training Method

Our training method is directly derived from optimization task (5). To enforce the 1-Lipshitz constraint on the critic (denoted as  $f$  in equation (3)), we use the gradient penalty version of WGAN [10]. That is, we train a generator  $G_{\theta}$  and a critic  $C_{\omega}$  (replacing  $f$ , to align with common WGAN notations) via the min-max optimization game

$$\min_{\theta} \max_{\omega} \mathbb{E}_{\mathbf{x}, \mathbf{y}} [\|\mathbf{x} - \mathbb{E}[G_{\theta}(\mathbf{z}, \mathbf{y})|\mathbf{y}]\|_2^2] + \lambda_{MM} \mathbb{E}_{\mathbf{x}, \mathbf{y}} [C_{\omega}(\mathbf{x}, \mathbf{y})] - \mathbb{E}_{\mathbf{z}, \mathbf{y}} [C_{\omega}(G_{\theta}(\mathbf{z}, \mathbf{y}), \mathbf{y})] + \lambda_{GP} \mathbb{E}_{\hat{\mathbf{x}}, \mathbf{y}} [(\|\nabla_{\hat{\mathbf{x}}} C_{\omega}(\hat{\mathbf{x}}, \mathbf{y})\|_2 - 1)^2], \quad (7)$$

where for a given  $\mathbf{y} = y$ , the last expectation is taken with respect to  $\mathbb{P}_{\hat{\mathbf{x}}}$ , the distribution of uniform samples along straight lines between pairs of points sampled from  $\mathbb{P}_{\mathbf{x}|\mathbf{y}=y}$  and  $\mathbb{P}_{\mathbf{g}_{\theta}|\mathbf{y}=y}$ . Our proposed training method is described in Algorithm 1 and we present our proposed generator architecture in Appendix A. Note that we evaluate the penalty term on the first 8 samples of each mini-batch of  $B = 32$  samples, and approximate  $\mathbb{E}[G_{\theta}(\mathbf{z}, \mathbf{y})|\mathbf{y}]$  by averaging  $M = 8$  generated samples for a given noisy image  $\mathbf{y}$ .

#### 3.2. A Denoiser with Two Distinct Capabilities

Recall that in our training method we drive our generator towards the production of samples from the posterior dis-

tribution while constraining the average denoised image to minimize the MSE. Thus, given such a trained model with enough capacity, the average denoised image of a given noisy input should approximately achieve the MMSE. This allows the optimized model to go beyond sampling from the posterior, producing an MMSE approximation result by averaging many generated samples. Even if the trained model does not accurately capture the true posterior, an average denoised image should produce low MSE, while the sampled denoised image should produce high perceptual quality. Our training method therefore allows one to obtain two denoisers at the same time: a denoiser that approximately samples from the posterior distribution and achieves high perceptual quality, and a denoiser that approximates the MMSE estimator. In Section 4, we refer to the former as *PSCGAN*, and to the latter as *PSCGAN-A*.

### 4. Experimental Evaluation

We turn to present an evaluation of our proposed generator architecture and training method on several data sets, and compare the performance with several other methods:

- DnCNN [32], a commonly accepted baseline.
- PSCGAN-A, which averages instances of PSCGAN.
- Ours-MSE, which is our proposed generator trained to solely optimize the MSE loss (without noise injections).

Evaluating the performance of PSCGAN and Ours-MSE allows us to better compare our proposed training method to an MSE based optimization procedure since we use the same architecture in both cases. In all experiments, the noise injected to the generator is of Gaussian distribution with zero mean. Moreover, when assessing PSCGAN, we vary at inference time the standard deviation of all noisy maps injected to the generator, which we denote as  $\sigma_{\mathbf{z}}$ . We also vary the number of instances produced by PSCGAN that are being averaged to compute PSCGAN-A (while keeping  $\sigma_{\mathbf{z}} = 1$ ), which we denote as  $N$ . The data sets we use are:

- FFHQ [15] thumbnails, 70,000 images. Images 3000-4999 use for testing and the rest for training.
- LSUN Bedroom [30], 3,037,042 images. The first 100,000 use for training and the last 4,042 for testing.
- LSUN Church [30], 126,227 images. The first 100,000 use for training and the last 4,227 for testing.

Our model assumes an input image of size  $128 \times 128$ , and since the images in both LSUN data sets are of size larger than  $128 \times 128$  in both axes, we first center crop each image while keeping the smaller dimension fixed, and then resize the resulting square image to  $128 \times 128$  through interpolation. In addition, we use random horizontal flip during training in all data sets. All denoising methods are assessed on images contaminated with different levels of additive white Gaussian noise with  $\sigma \in \{25, 50, 75\}$ . To clarify, we train a separate denoiser for each configuration of data set and

---

**Algorithm 1:** Training of the Posterior Sampling CGAN (PSCGAN).

---

**Require:** The gradient penalty coefficient  $\lambda_{GP}$ , the expected distance coefficient  $\lambda_{MM}$ , the number of critic iterations per generator iteration  $n_{critic}$ , the batch size  $B$ , the number of sampled realizations from the generator  $M$ , the penalty batch size  $PB$ , Adam hyperparameters  $\alpha, \beta_1, \beta_2$ , initial critic parameters  $\omega_0$ , and initial generator parameters  $\theta_0$ .

**Default Settings:**  $\lambda_{GP} = 10, \lambda_{MM} = 10^{-3}, n_{critic} = 1, B = 32, M = 8, PB = 8, \alpha = 10^{-3}, \beta_1 = 0, \beta_2 = 0.99$ .

**while**  $\theta$  has not converged **do**

```
    for  $t = 1, \dots, n_{critic}$  do
        for  $i = 1, \dots, B$  do
            Sample  $x \sim \mathbb{P}_x, z \sim \mathbb{P}_z, \epsilon \sim U[0, 1]$ 
             $y \leftarrow \text{deg}(x)$  // A stochastic degradation operator.
             $\tilde{x} \leftarrow G_\theta(z, y)$ 
             $\hat{x} \leftarrow \epsilon x + (1 - \epsilon)\tilde{x}$ 
             $L_C^{(i)} \leftarrow \lambda_{MM}(C_\omega(\tilde{x}, y) - C_\omega(x, y)) + \lambda_{GP}(\|\nabla_{\tilde{x}} C_\omega(\hat{x}, y)\|_2 - 1)^2$ 
         $\omega \leftarrow \text{Adam}(\nabla_\omega \frac{1}{B} \sum_{i=1}^B L_C^{(i)}, \omega, \alpha, \beta_1, \beta_2)$ 
    for  $i = 1, \dots, B$  do
        Sample  $x \sim \mathbb{P}_x, z^{(0)} \sim \mathbb{P}_z$ 
         $y \leftarrow \text{deg}(x)$ 
         $L_{G_{MM}}^{(i)} \leftarrow -\lambda_{MM} C_\omega(G_\theta(z^{(0)}, y))$ 
        if  $i \leq PB$  then
            Sample a batch  $\{z^{(j)}\}_{j=1}^M$ , each from  $\mathbb{P}_z$ 
             $L_{G_A}^{(i)} \leftarrow \|x - \frac{1}{M} \sum_{j=1}^M G_\theta(z^{(j)}, y)\|_2^2$ 
     $\theta \leftarrow \text{Adam}(\nabla_\theta \frac{1}{B} \sum_{i=1}^B L_{G_{MM}}^{(i)} + \frac{1}{PB} \sum_{i=1}^{PB} L_{G_A}^{(i)}, \theta, \alpha, \beta_1, \beta_2)$ 
```

---

noise level. The default hyperparameters we use to train PSCGAN (and consequently PSCGAN-A) are given in **Algorithm 1**. We train Ours-MSE and DnCNN to optimize the MSE loss using a batch size of 32, Adam optimizer with  $\beta_1 = 0.9, \beta_2 = 0.99$  and a learning rate of  $10^{-3}$ . The full implementation is publicly available.

#### 4.1. Perceptual Quality and Distortion Evaluation

In **Figure 1** we demonstrate the perceptual quality of several denoised images produced by our proposed method and by other MSE based methods on the FFHQ test set. The visual results produced on both LSUN test sets are in **Appendix B**. PSCGAN produces sharp and real looking results and outperforms the MSE methods in terms of perceptual quality, as the latter produce unnaturally smooth images.

Recall that PSCGAN is a stochastic denoiser able to produce many denoised outputs, and such variability is demonstrated in **Figure 2**. Even though the overall appearance of the varying samples is similar, we observe rich stochastic variation on fine details such as wrinkles, hair, eyes and more. In the same figure we also show the 4<sup>th</sup> root of the per-pixel standard deviation calculated on 32 denoised image samples of the same noisy input for each noise level. These results suggest that the penalty term in the optimization objective (5) indeed circumvents the aforementioned

mode collapse issue. In addition, it appears that our model does not suffer from inherent bias when handling skin tones, possibly due to the richness of the FFHQ data set [15].

To quantitatively evaluate our proposed method we use the Fréchet Inception Distance (FID) [11], which is known to correlate well with human opinion scores. Reliably computing FID requires a large amount of "real" samples (typically, at least 50,000), but evidently does not require many "fake" samples to remain consistent [17]. To confirm such evidence, we measure the FID<sup>1</sup> between each of our training sets and 100 randomly chosen subsets of 500 images taken from its corresponding test set, and see negligible variability in the reported scores. Thus, our procedure to measure the FID scores of each denoising algorithm is to consider its outputs on each test set (to its entirety) as the fake samples, and to use all of the clean images of the corresponding training set as the real ones. Since PSCGAN produces stochastic denoised images, we evaluate its average FID score by repeating this procedure 32 times, where in each time the FID is calculated with PSCGAN producing one sample of denoised image for each noisy input.

We report in **Table 1** the PSNR and FID scores obtained by all evaluated methods. It is important to note that, for a

---

<sup>1</sup>We use [22] to compute the FID.



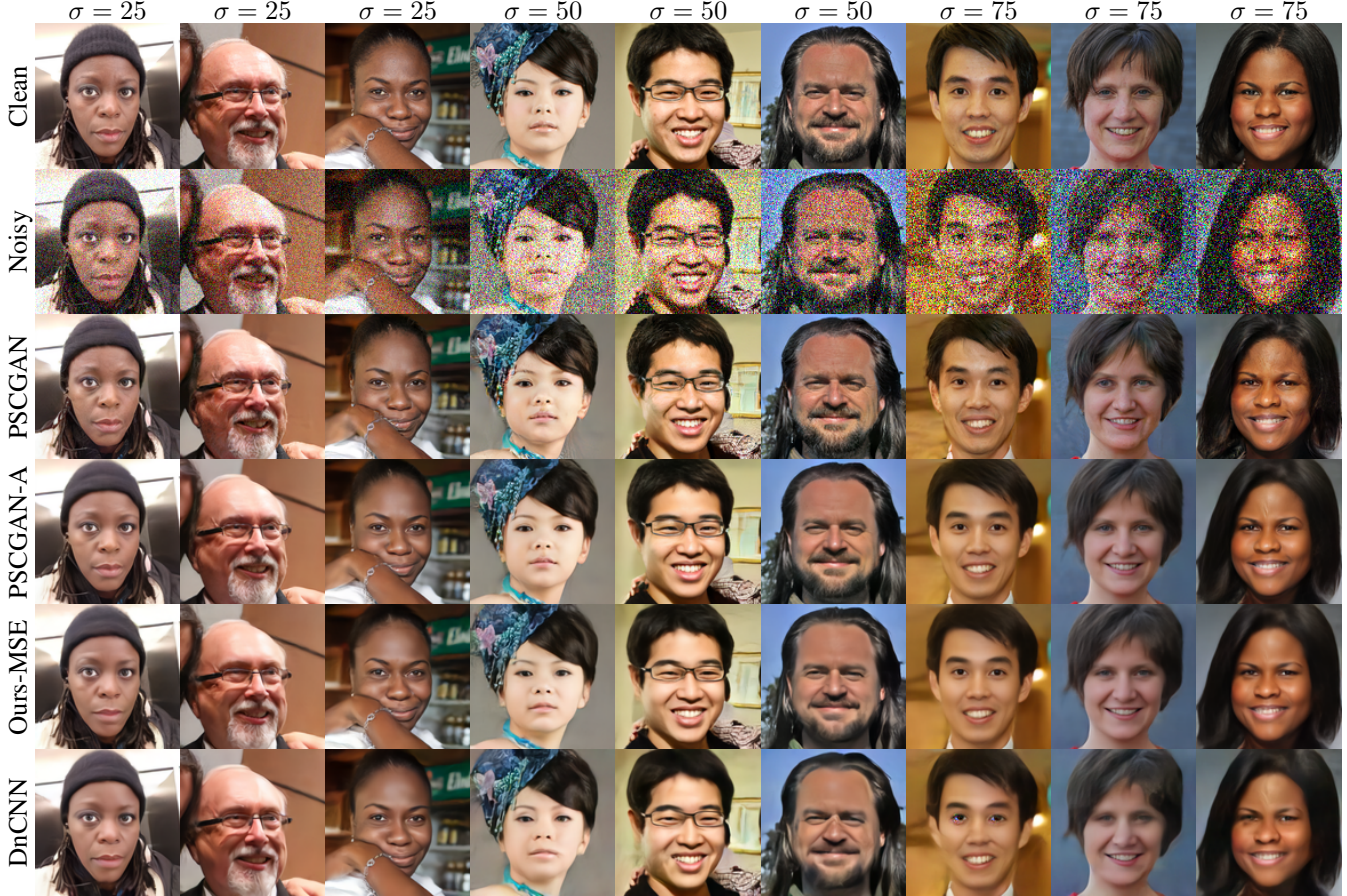


Figure 1: Denoising results on the FFHQ test set produced by several methods. PSCGAN is a sampled denoised image produced by our proposed method, attained by injecting noise with standard deviation of  $\sigma_z = 1$  (at both training and inference time). In this case, PSCGAN-A averages 64 instances of PSCGAN. Each model was trained on the FFHQ training set to denoise a specific noise level (25, 50 or 75).

fair comparison, we trained both DnCNN and our model on the same data sets, rather than using a pre-trained DnCNN model that is aimed to denoise an arbitrary natural image. Several observations and tendencies should be highlighted:

- As expected, in terms of PSNR, the best performing methods are the MMSE ones, with a gap of less than 3dB between these and PSCGAN, just as anticipated in [5].
- PSCGAN-A, which in this case averages 64 instances of PSCGAN, seem to provide a very good approximation for the MMSE denoiser in most cases.
- In terms of FID, our proposed method, PSCGAN, outperforms all other methods in all configurations, indicating that it indeed achieves superior perceptual quality.

#### 4.2. Traversing The Perception-Distortion Tradeoff

Our proposed method allows traversing the perception-distortion tradeoff in two ways: by varying  $\sigma_z$  or by varying  $N$ . We vary  $\sigma_z$  with values taken from  $\{0, 0.25, 0.5, 0.75, 1\}$ , and vary  $N$  with values taken from

$\{1, 2, 4, 8, 16, 32, 64\}$  (while fixing  $\sigma_z = 1$ ). We present the above traversals evaluated on the FFHQ test set in Figure 3, along with the FID and PSNR scores obtained by all evaluated MSE based methods. For PSCGAN we report the average FID scores and omit their standard deviations since they are negligible. In Figure 3 we observe that:

- As theoretically expected, PSCGAN-A approaches Ours-MSE as  $N$  increases (emphasized by the black dashed lines), which suggests that our training procedure was successful in satisfying the penalty term, since with the same architecture we see a comparable PSNR performance when solely optimizing the MSE.
- Varying  $N$  (while fixing  $\sigma_z = 1$ ) is more effective than varying  $\sigma_z$  (while fixing  $N = 1$ ), since each choice of  $\sigma_z$  is *dominated* [5] by some choice of  $N$ . We leave the explanation of this phenomenon for future research.
- The FID performance of PSCGAN is only slightly affected by the noise level, suggesting that our proposed method leads to high perceptual quality regardless of the





Figure 2: Stochastic variation of denoised images attained by 3 different generators, each trained with our proposed method to denoise images contaminated with noise levels of  $\sigma = 25, 50, 75$ . Two clean images are presented to the left, and their corresponding noisy versions to their right. Alongside each noisy input we show 4 examples of possible denoising outcomes, as well as the 4<sup>th</sup> root of the per-pixel standard deviation image calculated on 32 samples. For convenience, a gray-scale color map is added to the right (white and black correspond to low and high standard deviations, respectively). All denoised image samples were obtained by injecting noise with  $\sigma_z = 1$  at inference time.

noise contamination severity. This aligns with the posterior sampler’s property to always produce images with perfect perceptual quality [5]. In contrast, the PSNR performance of PSCGAN decreases as the noise level increases, which makes the perception-distortion tradeoff more significant in higher noise levels. This is emphasized by the two linear lines that diverge as the noise level increases. This evidence suggests that the gap in the perceptual quality of images produced by the posterior sampler and the MMSE estimator does not remain constant with the noise level, unlike the constant 3dB gap in PSNR [5].

### 4.3. Noise Reduction Evaluation

Image denoising is the process of recovering a clean signal  $\mathbf{x}$  from a noisy observation  $\mathbf{y}$ , where in our case,  $\mathbf{y} = \mathbf{x} + \mathbf{n}$  and  $\mathbf{n}$  is white Gaussian noise. This is an ill posed inverse problem and usually  $\mathbf{x}$  can not be fully retrieved. Thus, a *denoising algorithm* should find an approximation of  $\mathbf{x}$ , denoted as  $\hat{\mathbf{x}}$ , such that  $\mathbf{x}$  and  $\hat{\mathbf{x}}$  are close-by, and the *remainder noise*  $\hat{\mathbf{n}} = \mathbf{y} - \hat{\mathbf{x}}$  is white Gaussian. We now turn to assess whether PSCGAN, the algorithm which aims to sample from the posterior, satisfies such criteria.

The theoretical 3dB PSNR gap between the denoising results of a posterior sampler and of the MMSE estimator [5] guarantees that a well trained model that aims to sample from the posterior distribution would produce denoised images that are close to their clean sources, when closeness

Data set	$\sigma$	PSCGAN		PSCGAN-A		Ours-MSE		DnCNN	
		PSNR	FID	PSNR	FID	PSNR	FID	PSNR	FID
FFHQ	25	29.19	<b>12.66</b> $\pm$ 0.07	31.46	27.49	<b>31.64</b>	32.38	30.15	38.62
	50	25.84	<b>15.32</b> $\pm$ 0.10	28.28	32.06	<b>28.44</b>	41.56	28.30	42.96
	75	24.14	<b>15.90</b> $\pm$ 0.10	26.59	34.89	<b>26.8</b>	46.31	26.46	47.69
LSUN Bedroom	25	30.66	<b>9.24</b> $\pm$ 0.06	32.32	9.62	<b>32.61</b>	12.16	29.54	13.00
	50	27.35	<b>9.52</b> $\pm$ 0.07	29.12	11.22	<b>29.33</b>	12.77	29.13	21.61
	75	25.27	<b>11.78</b> $\pm$ 0.09	27.29	13.98	<b>27.46</b>	15.86	27.17	31.57
LSUN Church	25	29.02	<b>6.88</b> $\pm$ 0.03	30.76	8.48	<b>31.18</b>	8.76	31.15	9.41
	50	25.49	<b>8.43</b> $\pm$ 0.05	27.53	10.48	<b>27.76</b>	12.28	27.68	15.10
	75	23.74	<b>8.74</b> $\pm$ 0.07	25.83	12.02	<b>26.00</b>	14.41	25.77	21.21

Table 1: The PSNR (dB) and FID results obtained by several evaluated methods, each trained to denoise a specific noise level (higher PSNR and lower FID correspond to better performance). Notice that the reported PSNR is not the average one, but rather the PSNR calculated on the average MSE of the entire test set. PSCGAN is our sampler from the learned distribution, where we use  $\sigma_z = 1$  for the FFHQ test set and  $\sigma_z = 0.75$  for both LSUN test sets during inference. In this case, PSCGAN-A averages  $N = 64$  instances of PSCGAN (obtained with  $\sigma_z = 1$  on all data sets). Ours-MSE is our proposed generator trained to solely optimize the MSE loss (without noise injections). The FID reports of PSCGAN contain both the mean and the standard deviation (denoted with  $\pm$ ).

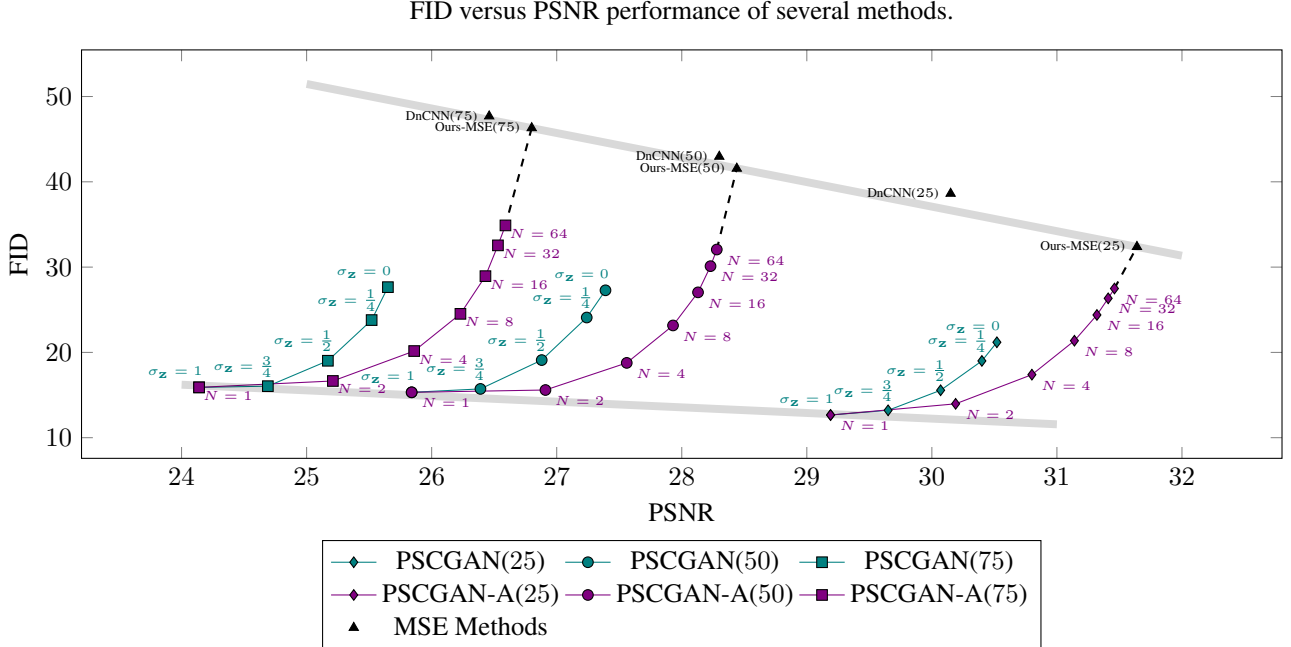


Figure 3: FID versus PSNR results for several methods: PSCGAN, PSCGAN-A that averages  $N$  instances of PSCGAN, Ours-MSE and DnCNN. The noise level ( $\sigma = 25, 50, 75$ ) is denoted with parentheses next to the name of each model. PSCGAN and PSCGAN-A are evaluated on different choices of  $\sigma_z$  and  $N$  during inference, respectively, while  $\sigma_z$  is fixed to 1 when varying  $N$ . The performance results of the MSE methods are also plotted. For more details, refer to [subsection 4.2](#).

is measured with MSE (as in most denoising algorithms). Although the PSNR results obtained by PSCGAN (Table 1) are indeed high, it clearly generates local content that is absent from the source image. Thus, we question whether the local patches of the reconstructed samples are still faithful to their clean counterparts. We measure the *patch-RMSE*,

the square root of the MSE between all overlapping clean and denoised patches of size  $15 \times 15$ , for all images in the FFHQ test set and for both PSCGAN and Ours-MSE. Finally, we create a histogram of the patch-RMSE values for each algorithm, and present the results in Figure 4. These give an approximation of the probability density function

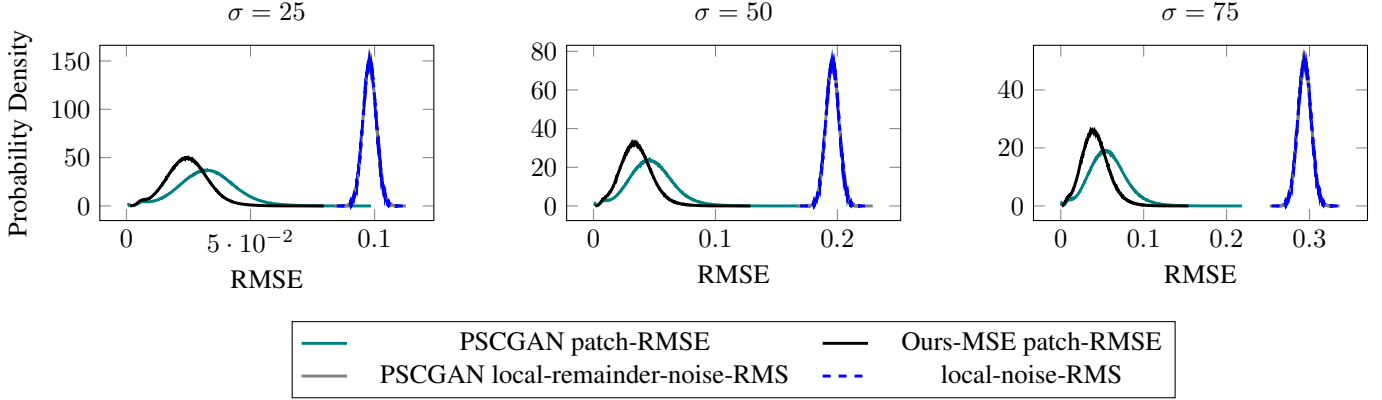


Figure 4: The approximated p.d.f of the patch-RMSE obtained by PSCGAN and by Ours-MSE, and of both the local-noise-RMS and the local-remainder-noise-RMS (obtained by Gaussian noise and by the remainder noise of PSCGAN, respectively).

(p.d.f) of the patch-RMSE values obtained by each method. In the same figure we also show the approximated p.d.f of the *local-noise-RMS*, the root mean square (RMS) value of all  $15 \times 15$  patches of the noise  $\mathbf{n}$  added to each ground truth image. Likewise, we also show the approximated p.d.f of the *local-remainder-noise-RMS*, referring to  $\hat{\mathbf{n}}$ . Observe that the patch-RMSE obtained by Ours-MSE and by PSCGAN approximately follow the same p.d.f shape but with different mean and standard deviation. Moreover, the p.d.fs of the local-noise-RMS and of the patch-RMSE obtained by PSCGAN are distant, and the mean of the former is much larger than that of the latter. Lastly, the p.d.f of the local-remainder-noise-RMS can not be distinguished from that of the local-noise-RMS. These results suggest that noise elimination is attained by PSCGAN even locally, which means that it is stable in the sense that it generally does not produce improper local details.

Next, we question whether the remainder noise is normally distributed. We use PSCGAN to denoise each image in the FFHQ test set and perform D’Agostino and Pearson’s normality test<sup>2</sup> [6] on all of the resulting remainder noise images (2000 noise images, each of size  $128 \times 128$ ). In addition, for each remainder noise image we extract randomly chosen  $15 \times 15$  patches and also patches that correspond to the largest patch-RMSE values (20 of each, for a total of  $20 \cdot 20 \cdot 2000$  patches), and assess if they are normally distributed as well. The results are reported in Table 2, and we see that PSCGAN successfully passes all tests, with a p-value of more than 0.05 with at least 94.6% confidence. This shows that the remainder noise by PSCGAN is normally distributed both locally and globally.

<sup>2</sup>A normally distributed random variable should have a p-value greater than a threshold  $\alpha$ . We use  $\alpha = 0.05$ , and in this case a realization of such a variable should pass the test with 95% confidence.

	$\sigma$	PSCGAN	Ours-MSE
<b>Global remainder noise</b>	25	95.4%	92.8%
	50	95.1%	94.5%
	75	95.1%	94.9%
<b>Worst patch-RMSE</b>	25	94.6%	94.2%
	50	94.8%	94.4%
	75	94.7%	94.8%
<b>Random patch-RMSE</b>	25	94.9%	94.6%
	50	94.7%	94.7%
	75	94.7%	94.6%

Table 2: The percentage of samples that passed the normality test. Global remainder noise is the full  $128 \times 128$  remainder noise image  $\hat{\mathbf{n}}$  produced by each algorithm. Worst patch-RMSE corresponds to the  $15 \times 15$  patches with the highest patch-RMSE values, taken from the remainder noise. Random patch-RMSE corresponds to randomly chosen patches taken from the remainder noise.

## 5. Summary

In this work, we revisit the image denoising task and focus on producing visually pleasing images, as opposed to distortion based methods, which target best PSNR. Our strategy relies on the perceptual quality and distortion guarantees of posterior sampling, and a novel design of a CGAN to meet these needs. We introduce a new constraint to the CGAN framework that alleviates its difficulty to train in the case of high dimensional distributions where each conditional input has only one corresponding source example. We propose a novel encoder-decoder denoiser architecture as well as a new training method, based on our theoretical formulation, which provide denoised images with high perceptual quality and acceptable distortion.



## 6. Acknowledgements

We thank Bahjat Kavar for his contribution to the development of this paper. We also thank Gennadi Zaidsher and the IT team of Technion’s CS Department for providing the resources conducting this research.

## References

- [1] Jonas Adler and Ozan Öktem. Deep bayesian inversion. *arXiv preprint arXiv:1811.05910*, 2018. 1, 2
- [2] Martin Arjovsky, Soumith Chintala, and Léon Bottou. Wasserstein generative adversarial networks. In Doina Precup and Yee Whye Teh, editors, *Proceedings of the 34th International Conference on Machine Learning*, volume 70, pages 214–223. PMLR, 2017. 1, 2
- [3] Yuval Bahat and Tomer Michaeli. Explorable super resolution. In *Proceedings of the IEEE Conference on Computer Vision and Pattern Recognition*, June 2020. 1
- [4] David Berthelot, Peyman Milanfar, and Ian Goodfellow. Creating high resolution images with a latent adversarial generator. *arXiv preprint arXiv:2003.02365*, 2020. 1, 2, 3
- [5] Yochai Blau and Tomer Michaeli. The perception-distortion tradeoff. *Proceedings of the IEEE Conference on Computer Vision and Pattern Recognition*, June 2018. 1, 3, 5, 6
- [6] Ralph D’Agostino and E. S. Pearson. Tests for departure from normality. empirical results for the distributions of  $b_2$  and  $\sqrt{b_1}$ . *Biometrika*, 60(3):613–622, 1973. 8
- [7] Ratnadeep Dey, Debotosh Bhattacharjee, and Mita Nasipuri. Image denoising using generative adversarial network. In J. K. Mandal and Soumen Banerjee, editors, *Intelligent Computing: Image Processing Based Applications*, volume 1157, pages 73–90. Springer Singapore, 2020. 1
- [8] Nithish Divakar and R. Venkatesh Babu. Image denoising via cnns: an adversarial approach. In *Proceedings of the IEEE Conference on Computer Vision and Pattern Recognition Workshops*, July 2017. 1
- [9] Ian Goodfellow et al. Generative adversarial nets. In Z. Ghahramani, M. Welling, C. Cortes, N. Lawrence, and K. Q. Weinberger, editors, *Advances in Neural Information Processing Systems*, volume 27, pages 2672–2680. Curran Associates, Inc., 2014. 1, 2
- [10] Ishaan Gulrajani et al. Improved training of wasserstein gans. In I. Guyon, U. V. Luxburg, S. Bengio, H. Wallach, R. Fergus, S. Vishwanathan, and R. Garnett, editors, *Advances in Neural Information Processing Systems*, volume 30, pages 5767–5777. Curran Associates, Inc., 2017. 1, 3
- [11] Martin Heusel, Hubert Ramsauer, Thomas Unterthiner, Bernhard Nessler, and Sepp Hochreiter. Gans trained by a two time-scale update rule converge to a local nash equilibrium. In *Proceedings of the 31st International Conference on Neural Information Processing Systems, NIPS’17*, page 6629–6640, Red Hook, NY, USA, 2017. Curran Associates Inc. 4
- [12] Phillip Isola, Jun-Yan Zhu, Tinghui Zhou, and Alexei A. Efros. Image-to-image translation with conditional adversarial networks. In *Proceedings of the IEEE Conference on Computer Vision and Pattern Recognition*, July 2017. 2
- [13] Tero Karras, Timo Aila, Samuli Laine, and Jaakko Lehtinen. Progressive growing of gans for improved quality, stability, and variation. *arXiv preprint arXiv:1710.10196*, 2018. 11
- [14] Tero Karras et al. Analyzing and improving the image quality of stylegan. In *Proceedings of the IEEE Conference on Computer Vision and Pattern Recognition*, June 2020. 1, 2, 11
- [15] Tero Karras, Samuli Laine, and Timo Aila. A style-based generator architecture for generative adversarial networks. In *Proceedings of the IEEE Conference on Computer Vision and Pattern Recognition*, June 2019. 1, 2, 3, 4
- [16] Mario Lucic et al. Are gans created equal? a large-scale study. In S. Bengio, H. Wallach, H. Larochelle, K. Grauman, N. Cesa-Bianchi, and R. Garnett, editors, *Advances in Neural Information Processing Systems*, volume 31, pages 700–709. Curran Associates, Inc., 2018. 1
- [17] Alexander Mathiasen and Frederik Hvilshøj. Fast fréchet inception distance. *arXiv preprint arXiv:2009.14075*, 2020. 4
- [18] Michael Mathieu, Camille Couprie, and Yann LeCun. Deep multi-scale video prediction beyond mean square error. *arXiv preprint arXiv:1511.05440*, 2016. 2
- [19] Sachit Menon et al. Pulse: Self-supervised photo upsampling via latent space exploration of generative models. In *Proceedings of the IEEE Conference on Computer Vision and Pattern Recognition*, June 2020. 1
- [20] Mehdi Mirza and Simon Osindero. Conditional generative adversarial nets. *arXiv preprint arXiv:1411.1784*, 2014. 1
- [21] O. Ronneberger, P. Fischer, and T. Brox. U-net: convolutional networks for biomedical image segmentation. In *Medical Image Computing and Computer-Assisted Intervention*, volume 9351 of *LNCS*, pages 234–241. Springer, 2015. 2, 11
- [22] Maximilian Seitzer. pytorch-fid: fid score for pytorch. <https://github.com/mseitzer/pytorch-fid>, August 2020. Version 0.1.1. 4
- [23] Yang Song et al. Score-based generative modeling through stochastic differential equations. In *International Conference on Learning Representations*, 2021. 1
- [24] Rini Thakur, R.N. Yadav, and Lalita Gupta. State-of-art analysis of image denoising methods using convolutional neural networks. *IET Image Processing*, 13, 08 2019. 1
- [25] Chunwei Tian et al. Deep learning on image denoising: an overview. *Neural Networks*, 131:251 – 275, 2020. 1
- [26] Francesco Tonolini et al. Variational inference for computational imaging inverse problems. *arXiv preprint arXiv:1904.06264*, 2020. 1
- [27] Gregory Vaksman, Michael Elad, and Peyman Milanfar. Lidia: lightweight learned image denoising with instance adaptation. In *The IEEE Conference on Computer Vision and Pattern Recognition Workshops*, June 2020. 1
- [28] Jay Whang, Erik M. Lindgren, and Alexandros G. Dimakis. Approximate probabilistic inference with composed flows. *arXiv preprint arXiv:2002.11743*, 2020. 1
- [29] Dingdong Yang et al. Diversity-sensitive conditional generative adversarial networks. In *Proceedings of the International Conference on Learning Representations*, 2019. 2

- [30] Fisher Yu et al. Lsun: construction of a large-scale image dataset using deep learning with humans in the loop. *arXiv preprint arXiv:1506.03365*, 2015. 3
- [31] Songhyun Yu, Bumjun Park, and Jechang Jeong. Deep iterative down-up cnn for image denoising. In *Proceedings of the IEEE Conference on Computer Vision and Pattern Recognition Workshops*, 2019. 1
- [32] Kai Zhang et al. Beyond a gaussian denoiser: residual learning of deep cnn for image denoising. *IEEE Transactions on Image Processing*, 26(7):3142–3155, 2017. 1, 3
- [33] Kai Zhang, Wangmeng Zuo, and Lei Zhang. Ffdnet: toward a fast and flexible solution for cnn-based image denoising. *IEEE Transactions on Image Processing*, 27(9):4608–4622, 2018. 1

# Appendices

## A. Generator (Denoiser) Architecture

Inspired by StyleGAN2 [14] and UNet [21], our conditional generator (denoiser) is an encoder-decoder deep neural network, as shown in Figure 5. The decoder builds the output image scale by scale by adding residual information at each stage to the up-sampled RGB output of the previous one. This approach was proposed in StyleGAN2 to sidestep the shortcomings of progressive growing [13, 14], a training methodology in which the number of layers in the generator and the discriminator increases during training. In the newly proposed scheme, both are trained end-to-end with all resolutions included, which significantly eases the training procedure but still enforces the decoder to progressively synthesize the output image stage-by-stage by adding resolution-specific details at each level. The encoder is analogous to a drip irrigation system. It consists of a main pipeline that has several exits to independent convolutional neural networks (CNNs), denoted as *drips*, each of which reinforces its neighboring decoder block with low receptive field information. The main pipeline is a deep CNN with high receptive field that progressively encodes the input image. This method alleviates the task of the decoder, especially at higher scales where original pixel locations are crucial for distortion performance.

Since our denoiser is stochastic and meant to sample from the posterior distribution, it can be considered as a mapping from the latent distribution of the random noise to the posterior, as in all GAN based sampling solutions. Instead of injecting a single noisy tensor to the first layer of our model, we inject noise at each scale of the decoder. These convolutional layers operate as follows: for a given layer with  $c$  input channels  $\{x_i\}_{i=1}^c$  and a random noise  $z$  of the same size, the resulting output of the layer (before the activation function is applied) is

$$\sum_{i=1}^c h_i * x_i + h_{c+1} * z,$$

where  $\{h_i\}_{i=1}^{c+1}$  are the convolutional kernels of the layer (considering only one block of kernels that leads to one output feature map). If one further assumes that  $h_{c+1} = \alpha$  (a 1-by-1 kernel) for some scaling factor  $\alpha$ , this boils down to the noise injection scheme presented in StyleGAN (each resulting feature maps corresponds to a different scaling factor). In addition, if one forces the scaling factors of all feature maps to be equal, this becomes the noise injection scheme presented in StyleGAN2. Thus, our scheme enlarges the hypothesis set of the convolution operating on  $z$ . As shown in Figure 5, we incorporate this idea by concatenating each noise injection to the next convolutional layer’s input.

## B. LSUN Data Sets’ Visual Results

In Figure 6 and Figure 7 we illustrate the visual quality of several denoised images produced by our method and by other MSE based methods on the LSUN Church and LSUN Bedroom test sets. As can be seen, our model produces denoised images with high perceptual quality, although in these data sets it is harder to notice the perceptual quality improvement with the naked eye (since the images are compressed).

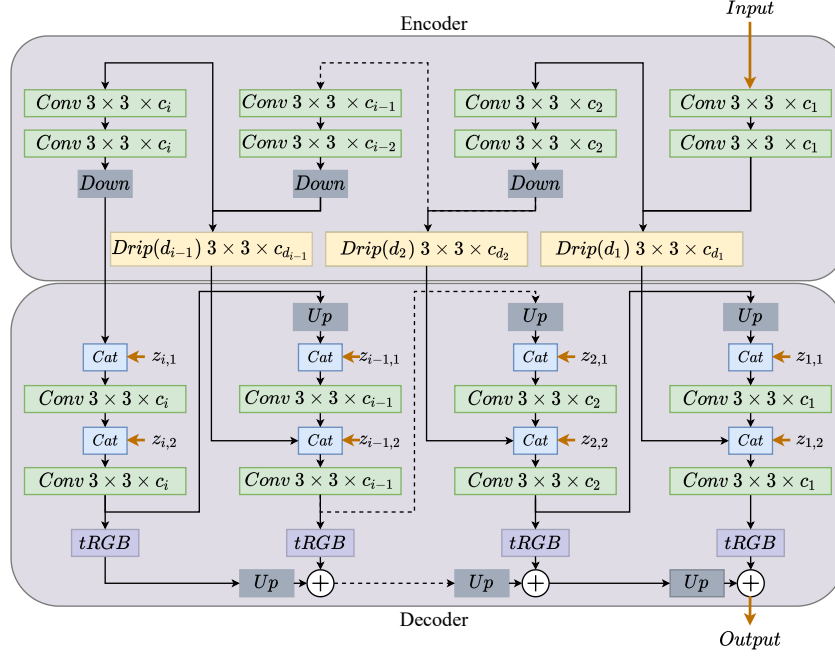


Figure 5: Our proposed generator architecture. An input noisy image is passed through an encoder of  $i$  doubly-blocked convolutional layers and downsampled after each. The downsampling operation is performed by a stride of 2 in the preceding convolution layer. The result of each doubly-blocked layer at index  $i$  is then passed through a *Drip*, which is a feed-forward CNN (in the figure,  $d_k$  and  $c_{d_k}$  denote the number of layers and the number of output channels of each layer in drip  $k$ , respectively). Each of these drips extracts features that are limited to a certain receptive field, which are then passed to the neighboring decoder block through concatenation. This further assists in reconstructing the RGB result of the corresponding scale, especially at higher scales. The decoder builds the reconstructed image scale by scale, using features aggregated both from previous layers of the decoder and the drip injections from the encoder. Noise injection is performed in the decoder’s pipeline, where a noisy “image”, denoted as  $z_{k,1}$  and  $z_{k,2}$  for each  $1 \leq k \leq i$ , is concatenated as another feature map of the input of the next layer. All convolutional layers, except for the  $tRGB$  layers, are coupled with Leaky ReLU activation functions.  $tRGB$  is a simple convolution operation with output channels being equal to the number of channels of the input image (usually 3). All up-sampling operations are performed with nearest-neighbor interpolation.



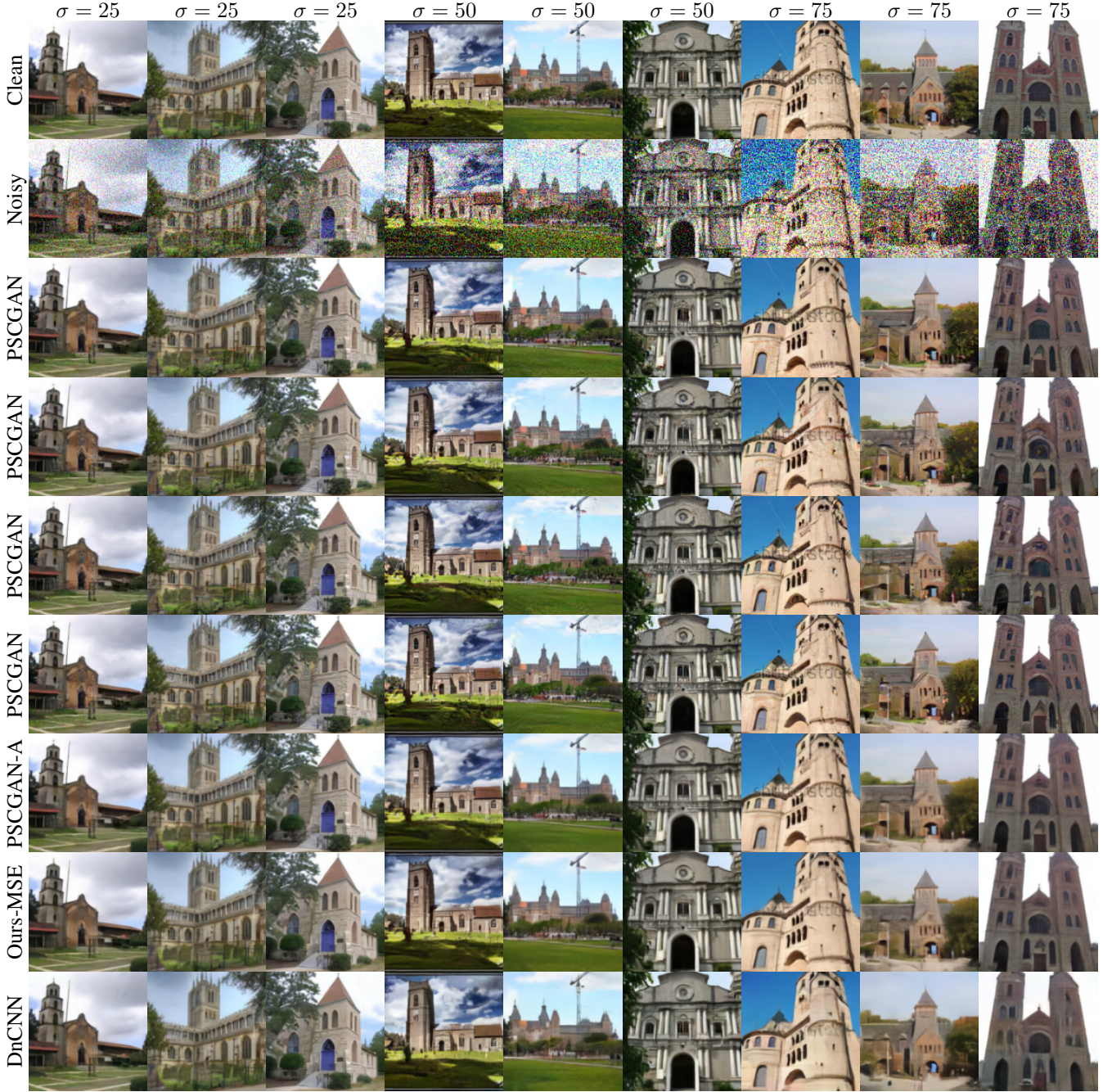


Figure 6: Denoising results on the LSUN Church test set produced by several methods. For each image we show four different outcomes of PSCGAN, each attained by injecting noise with standard deviation of  $\sigma_z = 0.75$ . PSCGAN-A averages 64 instances of PSCGAN. Each model was trained on the LSUN Church training set to denoise a specific noise level (25, 50 or 75).



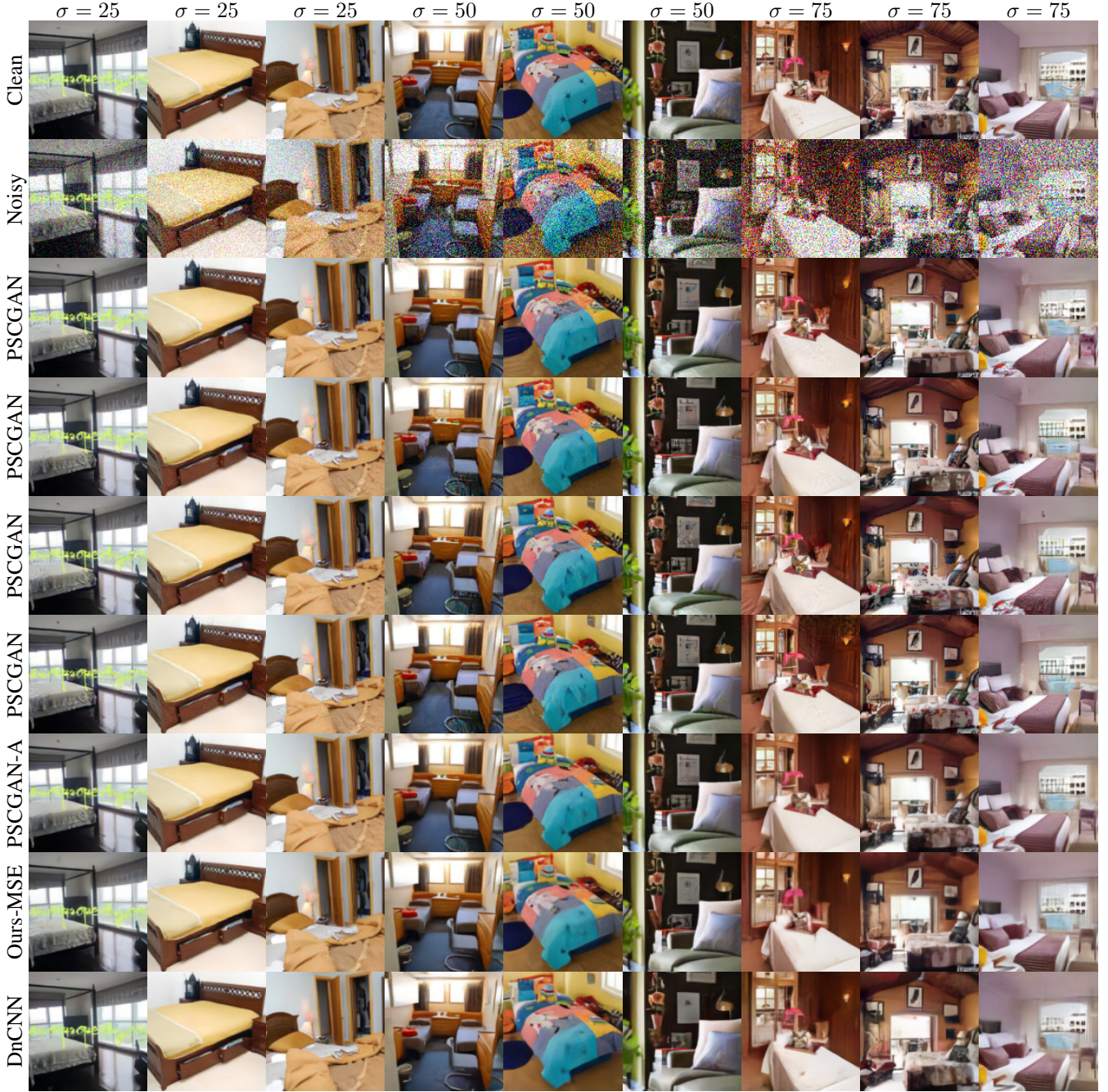


Figure 7: Denoising results on the LSUN Bedroom test set produced by several methods. For each image we show four different outcomes of PSCGAN, each attained by injecting noise with standard deviation of  $\sigma_z = 0.75$ . PSCGAN-A averages 64 instances of PSCGAN. Each model was trained on the LSUN Church training set to denoise a specific noise level (25, 50 or 75).